[Sensors] Manuscript ID: sensors-290680 - Accepted for Publication

April Zhu <april.zhu@mdpi.com>

2018-05-07 (월) 오후 1:08

받는 사람:Young Joo Lee (UEE) <ylee@unist.ac.kr>;

참
조: 이재범 (도시환경공학과/대학원생) <jblee@unist.ac.kr>; Kyoung-Chan Lee <kclee@krri.re.kr>; Sensors Editorial Office <sensors@mdpi.com>; April Zhu <april.zhu@mdpi.com>;

Dear Dr. Lee,

We are writing to you concerning the below referenced manuscript which you
submitted to the Sensors. Based on the completed set of reviews, the
manuscript has been accepted in its present format.

Manuscript ID: sensors-290680
Type of manuscript: Article
Title: Long-term deflection prediction from computer vision measured data
history for high-speed railway bridges
Authors: Jaebeom Lee, Kyoung-Chan Lee *, Young-Joo Lee *
Received: 25 March 2018
E-mails: jblee@unist.ac.kr, kclee@krri.re.kr, ylee@unist.ac.kr
Submitted to section: Physical Sensors,
http://www.mdpi.com/journal/sensors/sections/physicalsensors
Novel Methodologies to Interpret Non-Destructive Testing and Structural
Health Monitoring Data
http://www.mdpi.com/journal/sensors/special_issues/NDT_SHM
http://susy.mdpi.com/user/manuscripts/review_info/3d8a7c6dbfde8a847af8c725f82d5356

We will now edit and finalize your paper which will then be returned to you
for your approval. In order to shorten the processing time, it is important
for the authors to respond to the Production Staff in proofing stage within
48 hours of receiving the proof.

Congratulations on the acceptance of your manuscript, and thanks again for
your interest in submitting your work to Sensors.

If you have any questions, please contact MDPI Sensors Publication Office at
sensors@mdpi.com.

Ms. April Zhu
Assistant Editor
Sensors (http://www.mdpi.com/journal/sensors)

MDPI
Postfach, CH-4020 Basel, Switzerland
Office: St. Alban-Anlage 66, CH-4052 Basel, Switzerland
Tel.: +41 61 683 77 34; Fax: +41 61 302 89 18
http://www.mdpi.com/

Disclaimer: The information and files contained in this message are
confidential and intended solely for the use of the individual or entity to
whom they are addressed. If you have received this message in error, please
notify me and delete this message from your system. You may not copy this
message in its entirety or in part, or disclose its contents to anyone.

Long-term Deflection Prediction from Computer Vision Measured Data History for High-speed Railway Bridges

Jaebeom Lee [1], Kyoung-Chan Lee [2,*] and Young-Joo Lee [1,*]

[1] School of Urban and Environmental Engineering, Ulsan National Institute of Science and Technology (UNIST), Ulsan, 44919, Korea; jblee@unist.ac.kr (J. Lee), ylee@unist.ac.kr (Y.-J. Lee)

[2] Advanced Railroad Civil Engineering Division, Korea Railroad Research Institute, Uiwang, 16105, Korea; kclee@krri.re.kr

* Correspondence: kclee@krri.re.kr; ylee@unist.ac.kr

Abstract: Management of the vertical long-term deflection of a high-speed railway bridge is a crucial factor to guarantee traffic safety and passenger comfort. Therefore, there have been efforts to predict the vertical deflection of a railway bridge based on physics-based models representing various influential factors to vertical deflection such as concrete creep and shrinkage. However, it is not an easy task because the vertical deflection of a railway bridge generally involves several sources of uncertainty. This paper proposes a probabilistic method that employs a Gaussian process to construct a model to predict the vertical deflection of a railway bridge based on actual vision-based measurement and temperature. To deal with the sources of uncertainty which may cause prediction errors, a Gaussian process is modeled with multiple kernels and hyperparameters. Once the hyperparameters are identified through the Gaussian process regression using training data, the proposed method provides a 95% prediction interval as well as a predictive mean about the vertical deflection of the bridge. The proposed method is applied to an arch bridge under operation for high-speed trains in South Korea. The analysis results obtained from the proposed method show good agreement with the actual measurement data on the vertical deflection of the example bridge, and the prediction results can be utilized for decision-making on railway bridge maintenance.

Keywords: railway bridge; vertical deflection; probabilistic prediction; Gaussian process; training data

1. Introduction

Rail transport is one of the essential infrastructure systems that support human life and carry a large amount of freight and many passengers. Various research efforts have been devoted to develop faster and safer train systems, and as a result, high-speed trains, such as the Shinkansen in Japan, Inter City Express (ICE) in Germany, Train à Grande Vitesse (TGV) in France, and Korea Train eXpress (KTX) in Korea are in operation worldwide. In addition to the development of high-speed trains, the importance of building and managing railway structures that allow high-speed trains to operate safely has been recognized. Especially, managing the long-term vertical deflection of a bridge is essential for the traffic safety and passenger comfort of the high-speed trains.

In the case of a railway bridge, vertical deflection is one of the important indicators for inspecting its overall safety and for reporting abnormalities [1]. Moreover, it significantly influences the running stability of a train vehicle, particularly when traveling at high speed [2]. Therefore, keeping the vertical deflection of a railway bridge below a certain level is crucial for high-speed trains. Indeed, several standards, such as UIC CODE 518 OR (2009), Design Guide for Steel Railway Bridges of UK (2004), and Guideline of Track Maintenance of Korea Rail Network Authority (2016),

45 regulate guides to check the safety and comfort of rail traffic in terms of an acceptable vertical
46 deflection at mid-span [3−5].
47   Thus, many researchers have been trying to develop efficient sensors and methods to measure
48 the vertical deflection of railway bridges. A conventional contact type sensor is a linear variable
49 differential transformer (LVDT), which uses electric signals and has been used widely for structural
50 health monitoring [6]. However, it requires installing a device at a measurement point on a robust
51 platform of a bridge, which is often infeasible or impractical [7]. The accelerometer, which is
52 another widely used contact type sensor, does not require such installation. However, deflection
53 results based on accelerometers may have numerical errors, because the deflection calculation
54 requires the double integral of the measured acceleration [7]. To overcome the limitations of contact
55 type sensors, various non-contact type sensors, such as global positioning systems (GPS), laser
56 Doppler vibrometers (LDV), Radio Detection and Ranging (RADAR), and vision-based systems,
57 have also been developed. Although GPS, LDV, and RADAR can measure the vertical deflection of
58 a bridge accurately, they are relatively expensive [8−11].
59   On the other hand, vision-based systems, which use video images to measure the bridge
60 deflection, are widely used [7, 12, 13] because these systems are (1) relatively affordable; (2)
61 sufficiently precise for measuring the vertical deflection of bridges; (3) easy to install; (4) equipped
62 with small-sized and lightweight hardware; and (5) easy to upgrade by introducing a
63 high-frame-rate camera [14, 15]. Vision-based systems have been advanced in several aspects: target
64 or non-target approaches, feature detection, and coordinate transform algorithms [12]. In order to
65 detect features, the target-based approach utilizes a target marker which is attached to a structure
66 [12, 13, 16]; whereas the non-target-based approach uses features directly from a structure [7, 17].
67 For example, Lee *et al*. (2017) developed a target-based system [12], and Fukuda *et al*. (2013)
68 suggested a system without the installation of a target panel [7]. A more comprehensive review on
69 vision-based systems is provided by Lee *et al*. [12]. Despite the recent advances in vision-based
70 systems, the measurement results are also known to be affected by several factors such as
71 wind-shaking and camera location, which may produce measurement errors.
72   Meanwhile, research efforts have attempted to predict the vertical deflection of railway bridges,
73 and many of the previous studies focused on the derivation of physics-based models about the
74 vertical deflection [18−20]. Especially, prestressed concrete girders, which are often used for railway
75 bridges, are known to be deflected for various reasons including temperature changes, concrete
76 creep, shrinkage, and train loads. Thus, Guo *et al*. (2010) attempted to construct an equation to
77 mathematically represent the vertical deflection of a railway bridge by considering these physical
78 phenomena, and the actual measurement results were mainly used to validate the equation [18].
79 Similarly, Khan and Kim (2012) presented finite element model-based prediction on long-term
80 beam deflection which fitted to the experimental measurement [21]. Although the prediction on the
81 vertical deflection in these studies showed decent agreement with the actual measurement data, the
82 physics-based models need to be sophisticated when factors which were not considered in the
83 models need to be addressed [22]. In addition, most of the previous studies did not take into
84 account the uncertainty factors associated with railway bridges and could not give probabilistic
85 prediction on their vertical deflection [23].
86   Therefore, this study proposes a probabilistic method employing a Gaussian process (GP) to
87 predict the vertical deflection of a railway bridge based on actual vision-based measurement data
88 and temperature. The vision-based measurements of an example bridge were obtained using the
89 method of Kim and Kim (2014), in which a Digital Image Correlation (DIC) technique is introduced
90 to estimate the vertical deflection of a target [24−27]. To deal with the sources of uncertainty which
91 may cause prediction errors, the GP is modeled with multiple kernels and hyperparameters. Once
92 the hyperparameters are identified through GP regression using training data, the proposed method
93 provides the 95% prediction interval as well as the predictive mean of the vertical deflection of a
94 railway bridge.

95 **2. Proposed Method**

96   *2.1. Gaussian Process Regression*

97   This research aims to construct a probabilistic model to predict the vertical deflection of a
98   railway bridge, based on actual measurement data on vertical deflection and temperature. When a
99   prediction model is developed, in general, there are several sources of uncertainty related to the
100   model such as model misspecification, limited data size, and inherent variability, which are known
101   to introduce errors of bias, model variance, and noise into the model [28, 29]. Using the *prediction*
102   *error decomposition* proposed by Geman *et al*. (1992), the expectation of a squared prediction error
103   can be decomposed into these errors [30]. As model variance and bias occur because of
104   misspecification of the model or limited data size, these values are reducible. Meanwhile, noise
105   cannot be reduced because it occurs owing to inherent variability, and it is an irreducible error [31].
106   When constructing a prediction model, it is thus important to introduce an appropriate
107   mathematical model capable of addressing these three types of errors.

108   In this respect, many researchers have constructed probabilistic prediction models for their
109   engineering problems and tested these models by setting a confidence interval (CI) or a prediction
110   interval (PI) [32]. The term CI refers to an interval concerning only the reducible error (i.e., bias and
111   model variance). Meanwhile, the PI considers the irreducible error (i.e., noise) in addition to the
112   reducible error. This study aims to develop a probabilistic prediction model which can deal with
113   both of the reducible and irreducible errors and provide prediction results with a PI about the
114   vertical deflection of high-speed railway bridges.

115   To build a probabilistic prediction model, in this study, a GP is introduced. It is a machine
116   learning based method building a flexible Bayesian model [33], and it requires regression analysis to
117   identify appropriate GP parameters based on training data through optimization. The details of GPs
118   can be found in Rasmussen and Williams (2006) [34], and are briefly explained in this paper.

119   GPs are based on the Gaussian (i.e., normal) distribution, and a GP can be modeled by a
120   regression mean and a covariance matrix, which often requires high computational costs. Despite
121   their high costs, GPs have been widely utilized in many applications owing to their theoretical
122   simplicity and great performance to build a probabilistic model [34].

123   GPs are based on the following assumptions: 1) every data point is associated with a normally
124   distributed random variable; and 2) the finite collection of these random variables is multivariate
125   normally distributed, also explained as jointly normal. The multivariate normality is often
126   introduced to explain a set of correlated random data which cluster around the mean, and it
127   simplifies the related calculations with its definition that any sub-vector of the multivariate random
128   variables is again a Gaussian random vector [35]. For example, when one has a noisy training dataset
129   **D** from N_D times of measurement, which consists of a training input matrix **X** and a training output
130   vector **y**, the dataset can be expressed as

$$\mathbf{D} = \{(\mathbf{X}, \mathbf{y})\} = \left\{ (x_{ij}, y_i) \middle| i = 1, ..., N_D; j = 1, ..., N_x \right\} \tag{1}$$

131   where x_{ij} is an element of the training input matrix **X,** which is constructed from N_D times of
132   observation for N_x variables, and y_i is an element in the training output vector **y** whose size is N_D by 1.
133   Then, the two assumptions of GPs enable the prediction of the Gaussian mean and variance of the
134   output.

135   For a prediction purpose, when a test input matrix $\mathbf{X}_*$ is introduced to estimate the
136   corresponding unknown test output vector $\hat{f}_*(\cdot)$, the combined vector of the known training output
137   **y** and the unknown test output $\hat{f}_*(\cdot)$ is expressed as the multivariate Gaussian variables:

$$\begin{pmatrix} \mathbf{y} \\ \hat{f}_*\left(\mathbf{X}_*, \hat{\boldsymbol{\theta}}\right) \end{pmatrix} = N(\mathbf{O}, \Sigma) = N\left(\mathbf{O}, \begin{bmatrix} \mathbf{K} + \sigma_{noise}^2 \mathbf{I} & \mathbf{K}_* \\ \mathbf{K}_*^\mathbf{T} & \mathbf{K}_{**} + \sigma_{noise}^2 \mathbf{I} \end{bmatrix}\right) \tag{2}$$

138   where N denotes the multivariate Gaussian distribution, **O** is the zero matrix, which is often
139   introduced as a prior mean function for numerical simplicity [29, 33, 34], Σ is the symmetric and
140   positive semidefinite covariance matrix, **K** is the covariance matrix of the training input matrix **X**, $\mathbf{K}_*$

141 is the covariance matrix between training (**X**) and test (**X**∗) inputs, **K**∗∗ is the covariance matrix of the
142 test input matrix **X**∗, and σ_{noise}^2 is the variance of noise. In the covariance matrix Σ, noise is assumed
143 to be independent and identically normally distributed. Because the noise exists in the test data as
144 well as in the training data, the noise variance σ_{noise}^2 is added to all diagonal terms in the covariance
145 matrix Σ. When the sizes of the training input matrix and the test input are N_D by N_x and N_P by N_x,
146 respectively, the sizes of the covariance matrices **K**, **K**∗, **K**∗∗, and Σ are N_D by N_D, N_D by N_P, N_P by N_P,
147 and $(N_D + N_P)$ by $(N_D + N_P)$, respectively:

$$
\Sigma = \begin{bmatrix} \mathbf{K} + \sigma_{noise}^2 \mathbf{I} & \mathbf{K}_* \\ \mathbf{K}_*^{\mathbf{T}} & \mathbf{K}_{**} + \sigma_{noise}^2 \mathbf{I} \end{bmatrix} =
$$

$$
\begin{bmatrix} \begin{bmatrix} k(\mathbf{x}_1, \mathbf{x}_1) & \cdots & k(\mathbf{x}_1, \mathbf{x}_{N_D}) \\ \vdots & \ddots & \vdots \\ k(\mathbf{x}_{N_D}, \mathbf{x}_1) & \cdots & k(\mathbf{x}_{N_D}, \mathbf{x}_{N_D}) \end{bmatrix} & \begin{bmatrix} k(\mathbf{x}_1, \mathbf{x}_1^*) & \cdots & k(\mathbf{x}_1, \mathbf{x}_{N_P}^*) \\ \vdots & \ddots & \vdots \\ k(\mathbf{x}_{N_D}, \mathbf{x}_1^*) & \cdots & k(\mathbf{x}_{N_D}, \mathbf{x}_{N_P}^*) \end{bmatrix} \\ \begin{bmatrix} k(\mathbf{x}_1, \mathbf{x}_1^*) & \cdots & k(\mathbf{x}_1, \mathbf{x}_{N_P}^*) \\ \vdots & \ddots & \vdots \\ k(\mathbf{x}_{N_D}, \mathbf{x}_1^*) & \cdots & k(\mathbf{x}_{N_D}, \mathbf{x}_{N_P}^*) \end{bmatrix}^T & \begin{bmatrix} k(\mathbf{x}_1^*, \mathbf{x}_1^*) & \cdots & k(\mathbf{x}_1^*, \mathbf{x}_{N_P}^*) \\ \vdots & \ddots & \vdots \\ k(\mathbf{x}_{N_P}^*, \mathbf{x}_1^*) & \cdots & k(\mathbf{x}_{N_P}^*, \mathbf{x}_{N_P}^*) \end{bmatrix} \end{bmatrix} =
$$

$$
\begin{bmatrix} \begin{bmatrix} \sigma_{\mathbf{x}_1}^2 & \cdots & \sigma_{\mathbf{x}_1}\sigma_{\mathbf{x}_{N_D}}\rho_{\mathbf{x}_1\mathbf{x}_{N_D}} \\ \vdots & \ddots & \vdots \\ \sigma_{\mathbf{x}_{N_D}}\sigma_{\mathbf{x}_1}\rho_{\mathbf{x}_{N_D}\mathbf{x}_1} & \cdots & \sigma_{\mathbf{x}_{N_D}}^2 \end{bmatrix} & \begin{bmatrix} \sigma_{\mathbf{x}_1}\sigma_{\mathbf{x}_1^*}\rho_{\mathbf{x}_1\mathbf{x}_1^*} & \cdots & \sigma_{\mathbf{x}_1}\sigma_{\mathbf{x}_{N_P}^*}\rho_{\mathbf{x}_1\mathbf{x}_{N_P}^*} \\ \vdots & \ddots & \vdots \\ \sigma_{\mathbf{x}_{N_D}}\sigma_{\mathbf{x}_1^*}\rho_{\mathbf{x}_{N_D}\mathbf{x}_1^*} & \cdots & \sigma_{\mathbf{x}_{N_D}}\sigma_{\mathbf{x}_{N_P}^*}\rho_{\mathbf{x}_{N_D}\mathbf{x}_{N_P}^*} \end{bmatrix} \\ \begin{bmatrix} \sigma_{\mathbf{x}_1}\sigma_{\mathbf{x}_1^*}\rho_{\mathbf{x}_1\mathbf{x}_1^*} & \cdots & \sigma_{\mathbf{x}_1}\sigma_{\mathbf{x}_{N_P}^*}\rho_{\mathbf{x}_1\mathbf{x}_{N_P}^*} \\ \vdots & \ddots & \vdots \\ \sigma_{\mathbf{x}_{N_D}}\sigma_{\mathbf{x}_1^*}\rho_{\mathbf{x}_{N_D}\mathbf{x}_1^*} & \cdots & \sigma_{\mathbf{x}_{N_D}}\sigma_{\mathbf{x}_{N_P}^*}\rho_{\mathbf{x}_{N_D}\mathbf{x}_{N_P}^*} \end{bmatrix}^T & \begin{bmatrix} \sigma_{\mathbf{x}_1^*}^2 & \cdots & \sigma_{\mathbf{x}_1^*}\sigma_{\mathbf{x}_{N_P}^*}\rho_{\mathbf{x}_1^*\mathbf{x}_{N_P}^*} \\ \vdots & \ddots & \vdots \\ \sigma_{\mathbf{x}_{N_P}^*}\sigma_{\mathbf{x}_1^*}\rho_{\mathbf{x}_{N_P}^*\mathbf{x}_1^*} & \cdots & \sigma_{\mathbf{x}_{N_P}^*}^2 \end{bmatrix} \end{bmatrix}
$$

(3)

148 where **x**'s and **x**∗'s are the 1 by N_x vectors of training and test inputs, $k(\cdot)$ is an element termed the
149 *kernel* in the covariance matrix Σ, $\rho_{\mathbf{x}_a\mathbf{x}_b}$ is the correlation between $\mathbf{x}_a$ and $\mathbf{x}_b$, and $\sigma_{\mathbf{x}_a}^2$ is the variance
150 of $\mathbf{x}_a$.
151 In Equation (3), the covariance is often modeled by a *kernel* function associated with the
152 Euclidian distance between two inputs [34], and one popular choice of the *kernel* considering
153 correlation is the *squared exponential (SE) kernel* shown below:

$$
k_{SE}(\mathbf{x}_a, \mathbf{x}_b) = \sigma_f^2 \exp\left(-\frac{1}{2} \frac{\sqrt{\sum_{i=1}^{N_x} \left[\mathbf{x}_a(1,i) - \mathbf{x}_b(1,i) \right]^2}}{l^2} \right)
$$

(4)

154 where σ_f^2 is the variance hyperparameter of inputs which controls the vertical scale of the function
155 change and l is a length-scale hyperparameter that is associated with the horizontal scale of the
156 function change [29].
157 However, as shown in Equation (3), the covariance matrix Σ requires additional variance terms
158 for its diagonal terms (i.e., $\sigma_{noise}^2\mathbf{I}$). This study introduces the Kronecker delta function [34]:

$$
k_{var}(\mathbf{x}_a, \mathbf{x}_b) = \sigma_f^2 \cdot \delta(\mathbf{x}_a, \mathbf{x}_b)
$$

(5)

159 where $\delta(x_i,x_j)$ is the Kronecker delta function, which becomes one when the two inputs are the same,
160 and zero when they are different.
161   In other words, k_{SE} and k_{var} need to be introduced to construct the covariance matrix. Based on
162 this idea, a new kernel was proposed by summing up existing *kernels* without any loss of properties
163 as *kernel* [34]:

$$k(\mathbf{x}_a, \mathbf{x}_b) = \hat{\theta}_0 \exp\left(-\frac{1}{2}\frac{\sqrt{\sum_{i=1}^{N_x}\left[\mathbf{x}_a(1,i) - \mathbf{x}_b(1,i)\right]^2}}{\hat{\theta}_1^2}\right) + \hat{\theta}_2 \cdot \delta(\mathbf{x}_a, \mathbf{x}_b) + \hat{\theta}_3 \tag{6}$$

164 where $\hat{\theta}_0$ and $\hat{\theta}_1$ are hyperparameters for non-diagonal terms, $\hat{\theta}_2$ is a hyperparameter to control
165 the variance in diagonal terms, and $\hat{\theta}_3$ is a hyperparameter to control the level of the overall values
166 in the covariance matrix. The kernel in Equation (6) was applied to several previous studies [36−38],
167 and it is introduced to this study for building the covariance matrix in Equation (3).
168   A GP is sensitive to these hyperparameters; thus, for the purpose of prediction, the
169 determination of these parameters based on the given measurement data through optimization is
170 important to build an accurate prediction model. For the task, the concept of maximum likelihood is
171 often introduced [28].
172   Regarding Equations (1) and (2), the likelihood of observing the training output vector $\mathbf{y}$ given
173 the training input $\mathbf{X}$ can be expressed as a conditional probability using the multivariate normal
174 distribution as follows:

$$p(\mathbf{y}|X) = \frac{1}{(2\pi)^{\frac{N_D}{2}} \cdot |\mathbf{\Sigma}|^{\frac{1}{2}}} \cdot \exp\left(-\frac{1}{2}\mathbf{y}^T \mathbf{\Sigma}^{-1}\mathbf{y}\right) \tag{7}$$

175 For numerical convenience, the natural logarithm is introduced for conditional probability and is
176 multiplied by minus one:

$$L = -\ln p(\mathbf{y}|X) = \frac{1}{2}\mathbf{y}^T\left(\mathbf{K} + \sigma_{noise}^2\mathbf{I}\right)^{-1}\mathbf{y} + \frac{1}{2}\ln\left|\mathbf{K} + \sigma_{noise}^2\mathbf{I}\right| + \frac{N_D}{2}\ln(2\pi) \tag{8}$$

177 where L is the log-likelihood function. The three terms on the right in Equation (8) represent the
178 three errors in the prediction model described in Section 2.1 (i.e., the bias, model variance, and
179 noise).
180   Then, the best hyperparameters $\hat{\mathbf{\theta}}_{best}$ can be determined through optimization to minimize
181 the sum of these errors (i.e., the log-likelihood function L in Equation (8)):

$$\hat{\mathbf{\theta}}_{best} = \underset{\hat{\mathbf{\theta}}}{\arg\min}(L) \tag{9}$$

182 Since the conditional probability was multiplied by minus one as shown in Equation (8), $\hat{\mathbf{\theta}}_{best}$
183 obtained from the minimization problem in Equation (9) become the parameters which maximize
184 the likelihood of observing the training output vector $\mathbf{y}$ given the training input $\mathbf{X}$.
185   Once the hyperparameters are identified using Equation (9), the kernel in Equation (6) is
186 constructed. Then, the optimal covariance matrix in Equation (3) is composed and the mean and the
187 variance vectors of the test inputs can be calculated by the property of the multivariate Gaussian
188 distribution. Based on the derivation by Muirhead (2009), given test input $\mathbf{X}_*$, the conditional
189 multivariate Gaussian distributions of the test outputs $\hat{f}_*(\cdot)$ are estimated as follows [39]:

$$\hat{f}_*(\cdot)\Big|\mathbf{y}, \mathbf{X}, \mathbf{X}_* \sim N\left(\mathbf{K}_*^T\left(\mathbf{K} + \sigma_{noise}^2\mathbf{I}\right)^{-1}\mathbf{y}, \ \mathbf{K}_{**} - \mathbf{K}_*^T\left(\mathbf{K} + \sigma_{noise}^2\mathbf{I}\right)^{-1}\mathbf{K}_* + \sigma_{noise}^2\mathbf{I}\right) \tag{10}$$

190 Using Equation (10), the predictive mean and the PI can be estimated.

191   *2.2. Performance Assessment of Predictive Mean and Prediction Interval*

192   First, for the performance assessment of the predictive mean, a prediction error index is
193   defined. In this regard, the root-mean-square error (*RMSE*) has been widely used to quantify the
194   prediction error [40]:

$$RMSE = \sqrt{\frac{\sum_{i=1}^{N_p}(\hat{f}(\mathbf{x}_i) - y(\mathbf{x}_i))^2}{N_p}} \tag{11}$$

195   where $\hat{f}(\mathbf{x}_i)$ is the predictive mean at the test input $\mathbf{x}_i$ and $y(x_i)$ is the actual measurement.
196   Although the *RMSE* is a great test indicator of the predictive mean, it is also known to have
197   limitations for a fluctuating dataset, which can be easily found in the dataset of vertical deflection of
198   a railway bridge. A fluctuating dataset and the associated prediction, which is not overfitted and
199   follows the fluctuating trend, could have a large *RMSE* due to the inherent variability underlying
200   the data. For assessing how well the prediction follows the trend of the fluctuating dataset, the
201   mean-error (*ME*) is widely used as a good alternative indicator [41−43]:

$$ME = \frac{\sum_{i=1}^{N_p}(\hat{f}(\mathbf{x}_i) - y(\mathbf{x}_i))}{N_p} \tag{12}$$

202   Second, for the performance assessment of a PI, its coverage probability needs to be assessed
203   [32]. The coverage probability is generally defined by the percentage of actual measurement values
204   covered by a PI. A popular index is the PI coverage probability (*PICP*):

$$PICP = \frac{1}{N_p}\sum_{i=1}^{N_p} C_i \tag{13}$$

205   where C_i is the Boolean value which can be evaluated as:

$$C_i = \begin{cases} 1, & y_i \in [L_i, U_i] \\ 0, & y_i \notin [L_i, U_i] \end{cases} \tag{14}$$

206   where y_i is the ith measurement data, L_i is the lower bound, and U_i is the upper bound of the PI.
207   When all the measurement values are located in the PI, *PICP* becomes 1. In practice, the PI is built
208   with the nominal confidence of (1-α) %, which is known as the PI nominal confidence (*PINC*), and a
209   good PI should have a similar *PICP* with the given confidence level. In this respect, the average
210   coverage error (*ACE*) was defined with *PICP* and *PINC* as a performance measure of the PI [44]:

$$ACE = PINC - PICP \tag{15}$$

211   In this study, *RMSE* and *ME* are used to assess the performance of the predictive mean, and
212   *ACE* is introduced to estimate the performance of the PI.
213

3. Application Example

3.1. Example bridge: Eonyang Arch Bridge

216   The proposed method was applied to Eonyang Arch Bridge, which is a set of arch bridges for
217   high-speed trains and is located in Ulsan, South Korea. As shown in Figure 1, two twin bridges are
218   neighbored for north- and southbound traffic, respectively. The northbound bridge was used as the
219   test target structure in this study, and is shown in Figure 1.

Figure 1. Eonyang Arch Bridge.

Eonyang Arch Bridge was constructed in 2009 as a steel-concrete composite arch bridge for high-speed trains, the Korea Train Express (KTX), and Figure 2 shows its design drawings in the plan and front views. The bridge has a total length of 231.8 m, a center span of 70.4 m, a height of 10 m. Its substructure consists of three main arches rigidly connected to the foundation and several small arches over the main arch ribs. This unique structure consisting of main and small arches is designed to reduce the additional axial force of continuously welded rail on the bridge, and to provide a uniform level of stiffness over the entire bridge to enhance the comfort of passengers traveling in high-speed trains. Since the arch ribs are rigidly connected to the foundation, they deform vertically because of temperature change. The effect of this vertical deformation was evaluated for traffic safety and passenger comfort [45] and showed that upward deformation can adversely affect passenger comfort in hot weather over 40 degrees Celsius.

(a)

(b)
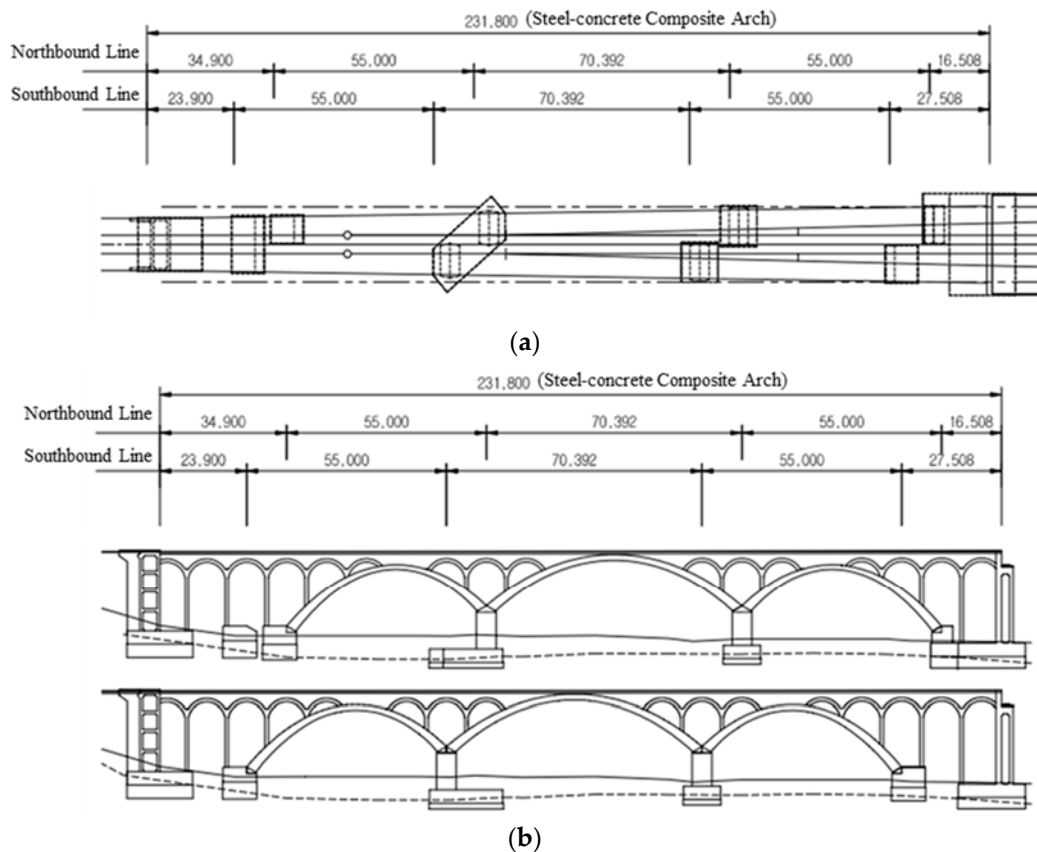
Figure 2. Design drawings of Eonyang Arch Bridge: (a) plan view; (b) front view.
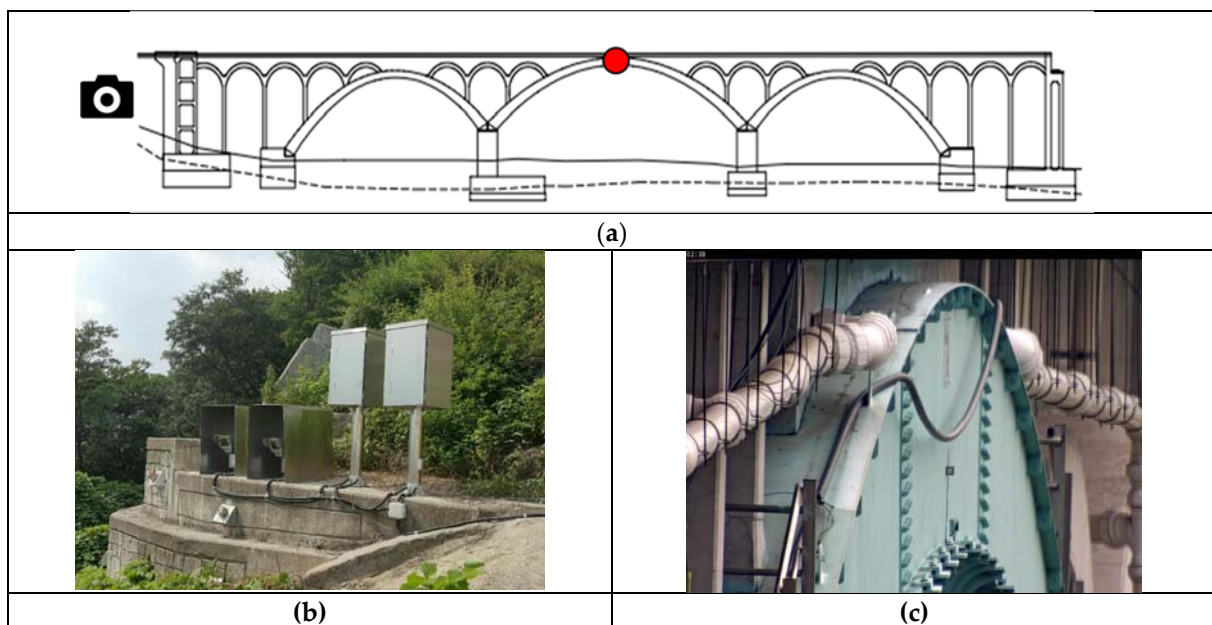
3.2. Measurement

The vertical deflection of Eonyang Arch Bridge and temperature were measured by the vision-based system and the Resistance Temperature Detector (RTD), respectively. First, the deflection at the center of the mid-span was measured as shown in Figure 3(a). Two HDTV video cameras were installed at a slope at the end of the bridge. The cameras have image sensors with progressive scan RGB CMOS 1/2" with 1920×1080 pixels and zoom lenses with focal lengths of 10-350 mm with a 35X zooming feature. The cameras were installed approximately 100 m from the bridge target and anchored to a concrete wall to minimize the movement of cameras as shown in Figure 3(b).

One camera was for measuring the deflection of the bridge and focused on a target installed at the web of the main arch crown. Figure 3(c) shows an example of an image captured by the camera. A preliminary measurement showed that the concrete wall at the slope showed some movement along with temperature change, which generated a large amount of noise during the vision measurement. As the target is 100 m from the camera, only 0.03 degree of vertical rotation of the camera can result in 50 mm of vertical deflection in the bridge. Therefore, even a small movement of the camera should be carefully corrected.

The other camera, which was for correcting the movement of the camera system, focused on a sign board installed at a building as a fixed reference point. Figure 3(d) shows a sign board image from the camera. If the concrete wall is displaced, the image of the fixed reference point from the building sign moves and the deflection from the first camera can be corrected by using this correcting movement. The algorithm used for the correction procedure is given in the previous study [27].

Second, the bridge temperatures were measured by using the Resistance Temperature Detector (RTD) in Figure 3(e), which can measure temperatures in the range from −50 to 100 degrees Celsius with a resolution of 0.5 degrees Celsius. The RTD sensor was installed on the inner side of the center span to avoid direct exposure to sunlight.

(a)

(b)

(c)

| (d) | (e) |

Figure 3. (**a**) Measurement location; (**b**) two video cameras; (**c**) bridge target video camera view for deflection measurement; (**d**) reference target video camera view for camera movement correction; (**e**) RTD and its installation.

Using the measurement systems, the vertical deflection and the bridge temperature were measured every 30 minutes for 4.5 months, from July 15 to November 27, 2016. Table 1 provides part of the results including the time, temperature, and deflection, and these were used as training data in this example. In Table 1, the time index is given in units of one day. Thus, it starts at 0.2500, which means 6:00 AM on July 15, 2016, and ends at 135.7292, which means the measurement was conducted for 135 days (i.e., 4.5 months). The positive and negative signs of the vertical deflection signify upward and downward deflection, respectively.

Table 1. Part of the measurement data on Eonyang Arch Bridge

| Training input data			Training output data
Measuring time	**Measuring time index [day]**	**Bridge temperature [°C]**	**Vertical deflection [mm]**
2016.7.15, 6:00	0.2500	21.45	1.195
2016.7.15, 6:30	0.2708	23.59	2.455
2016.7.15, 7:00	0.2917	25.73	3.565
...	...	...	...
2016.11.27, 16:00	135.6875	9.55	-6.127
2016.11.27, 16:30	135.7083	9.26	-6.638
2016.11.27, 17:00	135.7292	8.69	-7.300

The measurements that were recorded for 4.5 months produced a total of 2,292 datasets of the vertical deflection and bridge temperature, and they are plotted in Figure 4(a) and (b). Although there are some ranges without any data because the measurement devices malfunctioned, it is clearly observed that both of the vertical deflection and bridge temperature fluctuate with the same cycle within one day, which means the vertical deflection and bridge temperature are correlated. For this reason, in this example, a GP model is constructed with introducing temperature data as input.

Indeed, other factors than temperature such as creep, shrinkage, and train loads may also have an effect on the vertical deflection of a bridge. According to Nilson (2003), creep proceeds at a decreasing rate and ceases after two to five years at a final value and shrinkage continues at a decreasing rate for the first several months [46]. It was also stated by the American Concrete Institute (2008) that most of the shrinkage effects are manifested in the first year [47]. Because the example bridge was built in 2009 and the measurement was made in 2016, it was assumed in this study that the creep and shrinkage may not have a significant effect on the vertical deflection of the bridge. In addition, train load was not introduced as an important input in the example because

287 trains only remain on the bridge for a few seconds while passing one to two times per hour and it is
288 thus difficult to expect that a train would be passing at the moment when the bridge deflection is
289 being measured. For these reasons, in this example, the temperature is assumed to be the most
290 critical factor influencing the vertical deflection and is introduced as input.
291   Figure 4(c) clearly shows the positive correlation between the bridge temperature and vertical
292 deflection. Through regression analysis, the mean and 95% prediction intervals are obtain, and the
293 R-squared value is estimated to be 0.466, which means the temperature is an important factor
294 relating to vertical deflection. However, it also means there can be other influential factors which
295 were not measured in the experiment. Therefore, it is necessary to introduce probabilistic upper
296 and lower bounds of the output, when the prediction model is built using the temperature as input
297 data in this study.
298   When there is only one input as in this case, a simple regression can also give a mean equation
299 and confidence interval for lower costs. However, a GP model can provide more flexible predictive
300 mean and variance than regression [33, 34]. Furthermore, it enables the construction of a covariance
301 matrix with a kernel function in Equation (4) which decreases as the time interval increases. For
302 these reasons, GP is introduced to predict the vertical deflection in this example.
303

(a)

(b)

(**c**)
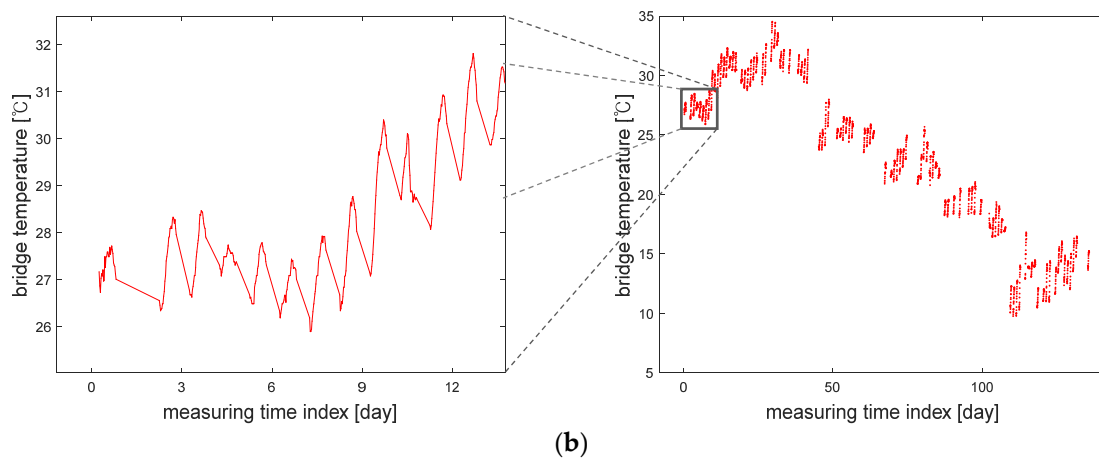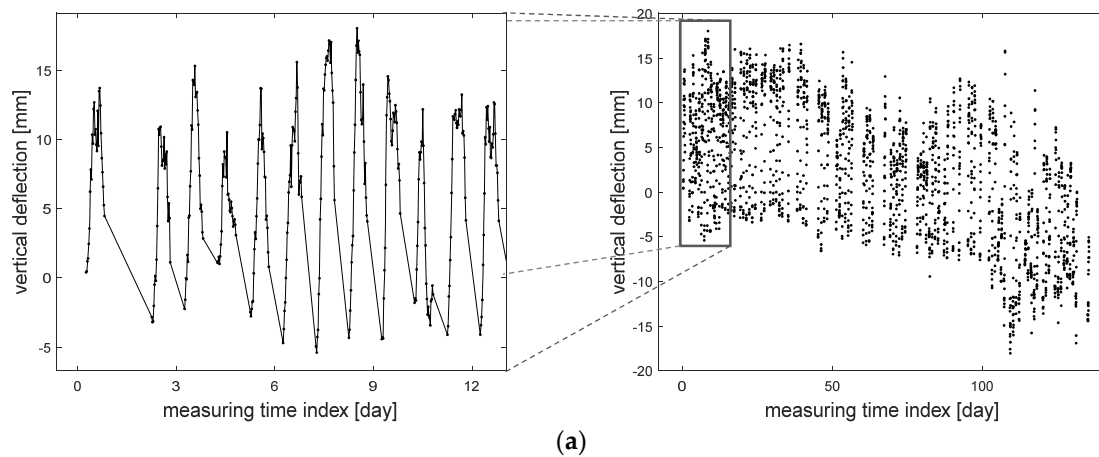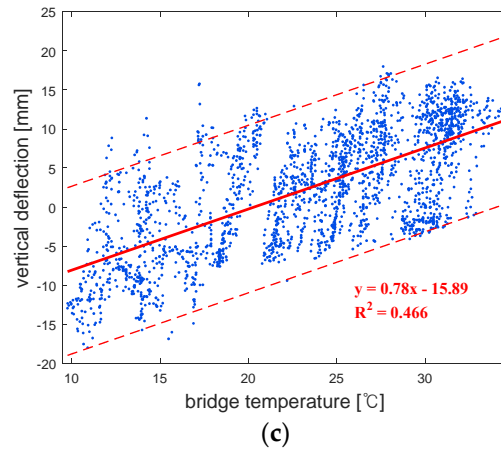
Figure 4. Measurement data: (**a**) vertical deflection; (**b**) bridge temperature; (**c**) bridge temperature versus vertical deflection.

For the construction of a GP model, the measuring time index and the bridge temperature are considered as input data to construct the training input matrix **X** in Equation (1), and the measured vertical deflection is used as output data in the same equation to construct the training output vector **y**. To predict the deflection based on the training data, the test input matrix **X**$_*$ in Equation (2) is constructed for the time of interest and the corresponding temperature, which were obtained from the database of the Korea Meteorological Administration [48].

4. Analysis Results

The vertical deflection of Eonyang Arch Bridge was predicted by using the proposed method and the measurement data for 4.5 months, and Figure 5 shows the results of predictive mean and 95% PI. As shown in the left figure, the actual measurement data on vertical deflection fluctuate on a daily basis, and the daily deflection ranges are approximately up to ±15 mm from the average. This is mainly because the vertical deflection is correlated with the temperature which also changes on a daily basis. In addition, as shown in the right figure, another cycle with a period of hundreds of days can be found in the prediction, which is thought to be due to the seasonal changes in the temperature.

Furthermore, Guideline of Track Maintenance of Korea (2016) suggests that, in the case of the example bridge, maintenance actions need to be taken when the absolute value of vertical deflection exceeds 18 mm [5]. Figure 5 shows that the measured absolute values are mostly smaller than the threshold, but there is a small probability of violating the regulation within the next few months. Thus, it is recommended to keep monitoring the vertical deflection, even though maintenance on the example bridge does not need to be done immediately.
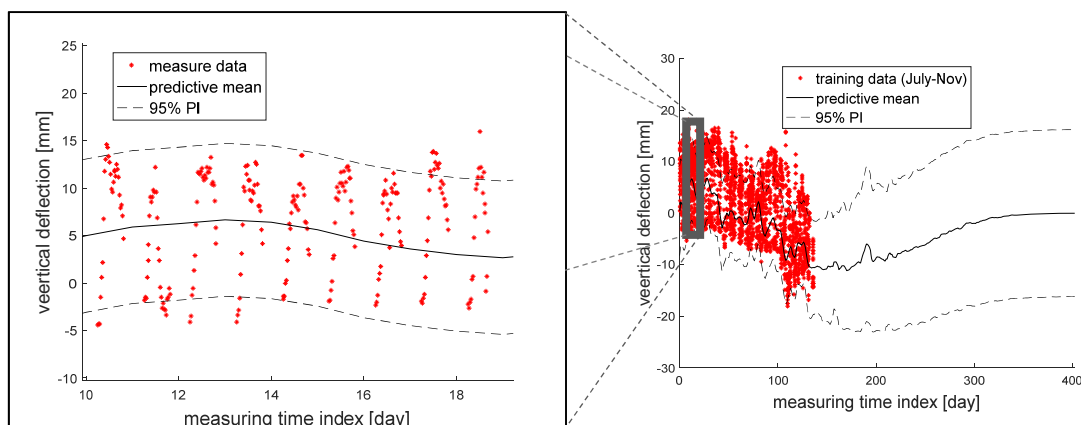
328 **Figure 5.** Analysis results of predictive mean and 95% PI from the entire measurement data (**right**)
329 and its zoom-in view (**left**).

330 To test the performance of the proposed method, predictions were made using different
331 durations of the measurement time as training data. In addition, actual measurement data that were
332 not included in the training data were used to validate the prediction results obtained from the
333 proposed method.
334 Figure 6 shows how the predictive mean and 95% PI are updated sequentially by additional
335 measurement data. For example, the black solid and dotted lines plotted in Figure 6(a) are
336 respectively the predictive mean and 95% PI obtained from the black measurement data in July,
337 2016 only. However, when blue additional data of the next month (i.e., August 2016) are also
338 considered for training, the predictive mean and 95% PI are updated in blue. Likewise, the
339 sequentially updated predictive means and 95% PIs after considering data in September, October,
340 and November are shown in Figures 6(b), 6(c), and 6(d), respectively.
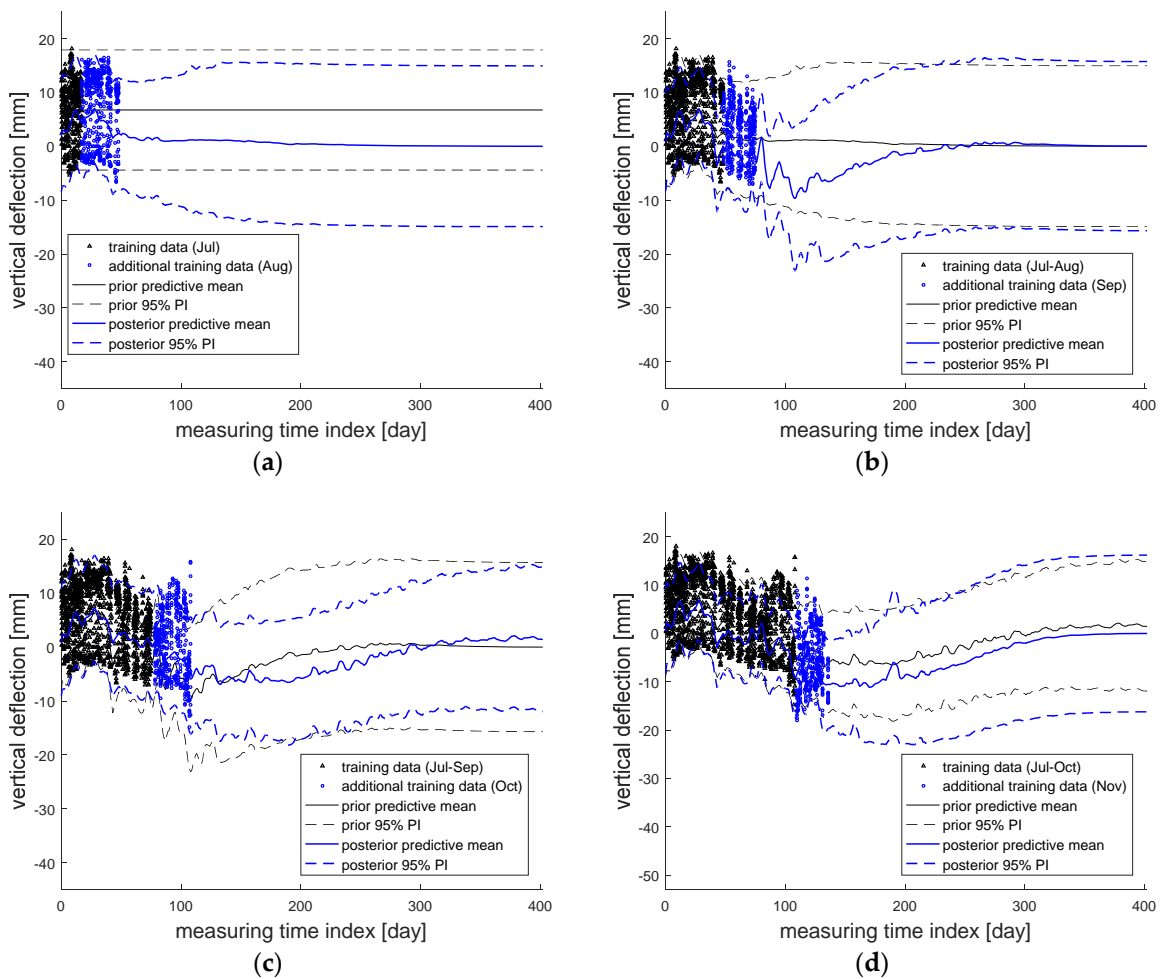
341 **Figure 6.** Sequentially updated predictive mean and 95% PI by adding the measurement data in: (**a**)
342 August; (**b**) September; (**c**) October; and (**d**) November.

343 The models constructed in Figure 6 were checked by calculating the *RMSE*s with respect to the
344 given datasets. Table 2 presents these results, and the *RMSE* values are estimated to be
345 approximately 5 mm overall, with minimum and maximum values of 4.01 mm and 6.20 mm,
346 respectively. As discussed in Section 2.2, the *RMSE* is calculated by comparing the predictive mean
347 and the actual measurement results every 30 minutes in this example, which means the overall 5
348 mm represents the inherent variability of the vertical deflection which cannot be reduced. In
349 addition, the *RMSE* values of 5 mm overall also mean the constructed models based on different
350 durations of measurement time have a similar level of inherent variability.

351 **Table 2.** *RMSE* values with respect to different sets of training data.

Given training data	Model of Jul. [mm]	Model of Jul.–Aug. [mm]	Model of Jul.–Sep. [mm]	Model of Jul.–Oct. [mm]	Model of Jul.–Nov. [mm]
Jul. 2016	4.01	4.09	4.60	4.28	4.71
Aug. 2016	-	5.43	5.58	5.39	5.66
Sep. 2016	-	-	4.78	4.24	4.21
Oct. 2016	-	-	-	5.89	6.2
Nov. 2016	-	-	-	-	4.49

352
353 These can be confirmed more clearly from Table 3, which shows the results of *ME* with respect
354 to the given datasets utilized for training. As shown in the table, the *ME* values are generally close
355 to zero, exactly in between −1.49 mm and 0.59 mm. This is because the inherent variabilities in the
356 prediction models are canceled out (as mentioned before), which means the prediction models are
357 close to being unbiased.

358 **Table 3.** *ME* values with respect to different sets of training data.

| Given training data	Model of Jul. [mm]	Model of Jul.–Aug. [mm]	Model of Jul.–Sep. [mm]	Model of Jul.–Oct. [mm]	Model of Jul.–Nov. [mm]
Jul. 2016	−0.84	−1.00	−1.04	−1.09	−0.81
Aug. 2016	-	0.29	−0.67	0.56	−0.93
Sep. 2016	-	-	−0.82	0.59	−0.26
Oct. 2016	-	-	-	−1.40	−1.49
Nov. 2016	-	-	-	-	−1.41

359
360 Meanwhile, Figure 7 compares the prediction results and the actual measurement data. For
361 example, Figure 7(a) shows the predictive mean and 95% PI (in black) based on the measurement
362 data in July only and compares them with the actual measurement data obtained from August
363 through November. It is clearly seen that the prediction accuracy gradually decreases as the
364 moment of prediction moves farther away. However, as the duration of the measurement time for
365 training data becomes longer, more accurate prediction models are obtained, and the prediction
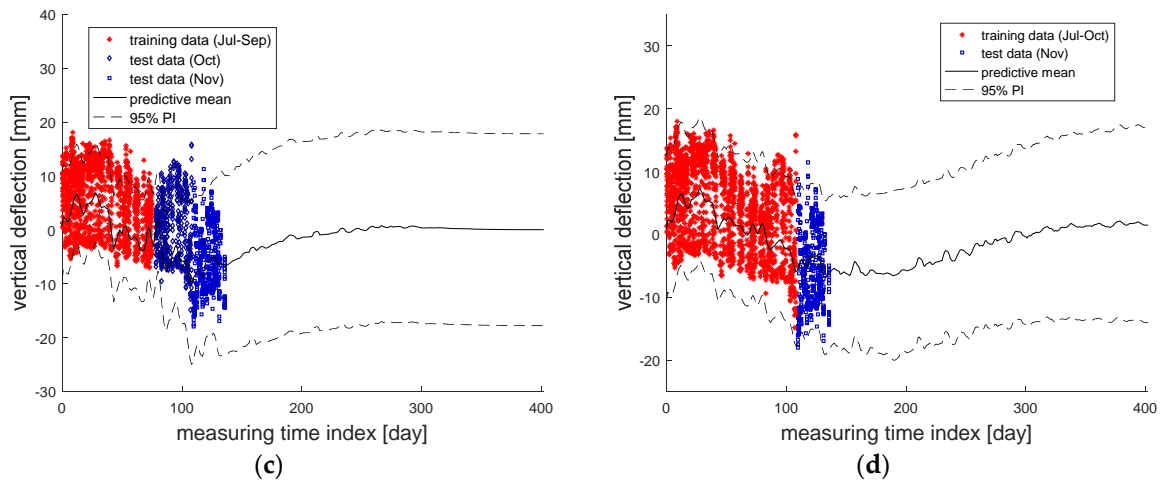366 results become quite similar to the actual measurement data.
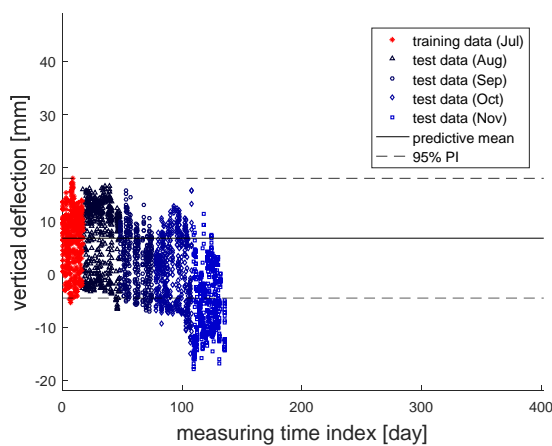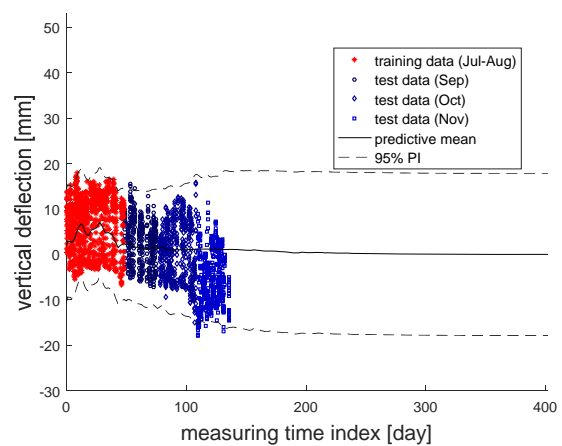
Figure 7. Comparison between the actual measurement data and the prediction results based on the datasets within: (**a**) July; (**b**) Jul. to Aug.; (**c**) Jul. to Sep.; (**d**) Jul. to Nov.

These points can be observed more clearly using performance assessment indices. Table 4 shows the *RMSE* values with respect to different sets of test data. From the table, it is first seen that the *RMSE* values are relatively small when the prediction results are compared with the measurement data of the subsequent months and the *RMSE* values increase as the moment of prediction moves farther away. Second, it is also observed that the *RMSE* values decrease as measurement data for a longer duration is used.

Table 4. *RMSE* values with respect to different sets of test data.

Given test data	Model of Jul. [mm]	Model of Jul.–Aug. [mm]	Model of Jul.–Sep. [mm]	Model of Jul.–Oct. [mm]	Model of Jul.–Nov. [mm]
Jul. 2016	-	-	-	-	-
Aug. 2016	6.82	-	-	-	-
Sep. 2016	7.55	3.98	-	-	-
Oct. 2016	7.97	5.27	4.29	-	-
Nov. 2016	12.28	7.06	3.35	3.42	-

These findings are more evident with *ME*, where the inherent variabilities are canceled out. Table 5 provides the results of *ME* with respect to different sets of test data. As shown in the table, although the model that was constructed based only on the measurement data in July may seem acceptable for August with 2.36 mm, the *ME* values continue increasing as the moment for prediction is taken farther away from the measurement period (i.e., July). However, whenever an additional dataset is added to the training data, the absolute *ME* value generally decreases, which means the accuracy of the prediction model improves. For example, the *ME* value of the prediction model constructed using the data from July to October has a small *ME* value of 0.49 mm, when the model is compared with the actual measurement data for November.

Table 5. *ME* values with respect to different sets of test data.

Given test data	Model of Jul. [mm]	Model of Jul.–Aug. [mm]	Model of Jul.–Sep. [mm]	Model of Jul.–Oct. [mm]	Model of Jul.–Nov. [mm]
Jul. 2016	-	-	-	-	-
Aug. 2016	2.36 mm	-	-	-	-

Sep. 2016	6.76 mm	1.73 mm	-	-	-
Oct. 2016	5.94 mm	0.37 mm	−1.47 mm	-	-
Nov. 2016	11.82 mm	6.22 mm	−1.66 mm	0.49 mm	-

On the other hand, to check the results of 95% PIs, the *ACE* values are calculated with respect to the given dataset. Table 6 shows the *ACE* values with respect to different sets of training data, and it can be seen that the *ACE* values are close to zero overall. This means the PI of each prediction model covers the specified portion (i.e., 95% in this example) of the given data.

Table 6. *ACE* values with respect to different sets of training data.

Given training data	Model of Jul. [mm]	Model of Jul.–Aug. [mm]	Model of Jul.–Sep. [mm]	Model of Jul.–Oct. [mm]	Model of Jul.–Nov. [mm]
Jul. 2016	−0.0411	0.0170	−0.0165	0.0125	−0.0188
Aug. 2016	-	−0.0045	0.0285	−0.0293	0.0120
Sep. 2016	-	-	0.0104	−0.0379	−0.0065
Oct. 2016	-	-	-	0.0474	0.0460
Nov. 2016	-	-	-	-	−0.0197

In addition, Table 7 presents the *ACE* values with respect to different sets of test data. The two facts that were already observed with *RMSE* and *ME* are clearly noticeable. First, it is seen that *ACE* values are relatively small when the PIs are compared with the measurement data of the subsequent months and the absolute values of *ACE* increase as the moment of prediction moves farther away. Second, it is also observed that the absolute values of *ACE* decrease as measurement data for a longer duration are used.

Table 7. *ACE* values with respect to the test datasets.

Given test data	Model of Jul. [mm]	Model of Jul.–Aug. [mm]	Model of Jul.–Sep. [mm]	Model of Jul.–Oct. [mm]	Model of Jul.–Nov. [mm]
Jul. 2016	-	-	-	-	-
Aug. 2016	−0.0335	-	-	-	-
Sep. 2016	0.0273	−0.0258	-	-	-
Oct. 2016	0.2248	−0.0397	0.0460	-	-
Nov. 2016	0.5864	0.0482	−0.0478	−0.0284	-

5. Conclusions

This paper proposes a probabilistic method which employs a Gaussian process to construct a model to predict the vertical deflection of a railway arch bridge based on actual computer vision measured data. To deal with the sources of uncertainty which may cause errors in a prediction model, a Gaussian process is modeled with multiple kernels and hyperparameters. Once the hyperparameters are identified through the Gaussian process regression using training data, the proposed method provides the predictive mean and 95% prediction interval of the vertical deflection of the target bridge. The proposed method was tested by applying it to Eonyang Arch Bridge, which is a railway bridge operated for high-speed trains in South Korea. The corresponding analysis results showed that as additional training data were introduced, both the predictive mean and predictive interval could be updated. In addition, the analysis results of predictive mean and 95%

413   PI obtained from the proposed method showed good agreement with the actual measurement data
414   on the vertical deflection of the example bridge, and it was shown that the prediction results could
415   be utilized for decision-making on railway bridge maintenance.

418   **Author Contributions:** Jaebeom Lee developed the proposed method and performed the probabilistic analysis.
419   Young-Joo Lee co-developed the proposed method and guided this research overall. Kyoung-Chan Lee
420   designed the application example, carried out the measurement on the example bridge, and extracted the
421   vertical deflection results from the measurement data.

References

423   1.   Chung, W.; Kim, S.; Kim, N.S.; Lee, H.U. Deflection estimation of a full scale prestressed concrete girder
424   using long-gauge fiber optic sensors. *Construction and Building Materials* **2008**, 22, 394-401.

425   2.   Guo, T.; Liu, T.; Li, A. Deflection reliability analysis of PSC box-girder bridge under high-speed railway
426   loads. *Advances in Structural Engineering* **2012**, 15, 2001-2011.

427   3.   International Union of Railways *Testing and approval of railway vehicle from the point of view of their dynamic*
428   *behavior-safety-track fatigue-ride quality*, 4th edition, UIC CODE 518 OR. **2009**.

429   4.   Iles, D.C. *Design guide for steel railway bridges*. Berkshire, UK: Steel Construction Institute **2004**.

430   5.   Korea Rail Network Authority *Guideline of Track Maintenance*. **2016**.

431   6.   Cho, S.; Sim, S.H.; Park, J.W.; Lee, J. Extension of indirect displacement estimation method using
432   acceleration and strain to various types of beam structures. *Smart Structures and Systems* **2014**, 14, 699-718.

433   7.   Fukuda, Y.; Feng, M.Q.; Narita, Y.; Kaneko, S.I.; Tanaka, T. Vision-based displacement sensor for
434   monitoring dynamic response using robust object search algorithm. *IEEE Sensors Journal* **2013**, 13,
435   4725-4732.

436   8.   Wahbeh, A.M.; Caffrey, J.P.; Masri, S.F. A vision-based approach for the direct measurement of
437   displacements in vibrating systems. *Smart materials and structures* **2003**, 12, 785-794.

438   9.   Gentile, C.; Cabboi, A. Vibration-based structural health monitoring of stay cables by microwave remote
439   sensing. *Smart Struct. Syst.* **2015**, 16(2), 263-280.

440   10.   Castellini, P.; Martarelli, M.; Tomasini, E.P. Laser Doppler Vibrometry: Development of advanced
441   solutions answering to technology's needs. *Mechanical Systems and Signal Processing* **2006**, 20, 1265-1285.

442   11.   Ribeiro, D.; Calçada, R.; Ferreira, J.; Martins, T. Non-contact measurement of the dynamic displacement
443   of railway bridges using an advanced video-based system. *Engineering Structures* **2014**, 75, 164-180.

444   12.   Lee, J.; Lee, K.-C.; Cho, S.; Sim, S.-H. Computer vision-based structural displacement measurement robust
445   to light-induced image degradation for in-service bridges. *Sensors* **2017**, 17(10), 2317.

446   13.   Vicente, M.A.; Gonzalez, D.C.; Minguez, J.; Schumacher, T. A Novel Laser and Video-Based
447   Displacement Transducer to Monitor Bridge Deflections. *Sensors* **2018**, 18(4), 970.

448   14.   Zhao, X.; Liu, H.; Yu, Y.; Xu, X.; hu, W.; Lo, M.; Ou, J. Bridge displacement monitoring method based on
449   laser projection-sensing technology. *Sensors*, **2015**, 15(4), 8444-8463.

450   15.   Artese, S.; Achilli, V.; Zinno, R. Monitoring of Bridges by a Laser Pointer: Dynamic Measurement of
451   Support Rotations and Elastic Line Displacement: Methodology and First Test. *Sensors (Basel, Switzerland)*,
452   **2018**, 18(2)

453   16.   Feng, D.; Feng, M.Q.; Ozer, E.; Fukuda, Y. A vision-based sensor for noncontact structural displacement
454   measurement. *Sensors* **2015**, 15(7), 16557-16575.

455   17.   Feng, M.Q.; Fukuda, Y.; Feng, D.; Mizuta, M. Nontarget vision sensor for remote measurement of bridge
456   dynamic response. *Journal of Bridge Engineering* **2015**, 20(12), 04015023.

457   18.   Guo, T.; Sause, R.; Frangopol, D.M.; Li, A. Time-dependent reliability of PSC box-girder bridge
458   considering creep, shrinkage, and corrosion. *Journal of Bridge Engineering* **2010**, 16, 29-43.

459   19.   Bažant, Ž.; Yu, Q.; Li, G.H. Excessive long-time deflections of prestressed box girders. II: Numerical
460   analysis and lessons learned. *Journal of structural Engineering* **2012**, 138, 687-696.

461   20.   Kamatchi, P.; Rao, K.B.; Dhayalini, B.; Salibabu, S.; Parivallal, S.; Ravisankar, K.; Iyer, N.R. Long-term
462   prestress loss and camber of box-girder bridge. *ACI Structural Journal* **2014**, 111, 1297-1306.

463   21.   Khan, F.; Kim, Y.J. Time-dependent and residual behavior of pultruded GFRP beams subjected to
464   sustained intensities and cold temperature. *Cold Regions Science and Technology* **2012**, 74, 43-51.

22. Wu, B.; Lu, H.; Chen, B.; Gao, Z. Study on finite element model updating in highway bridge static loading test using spatially-distributed optical fiber sensors. *Sensors* **2017**, 17(7), 1657.

23. Beltempo, A.; Bursi, I. S.; Cappello, C.; Zonta, D.; Zingales, M. A. Viscoelastic model for the long-term deflection of segmental prestressed box girders. *Computer-Aided Civil and Infrastructure Engineering* **2017**, 00, 1-15.

24. Kim, S.-W. Health monitoring of civil structures using vision-based measurement system. Pusan National University. **2014**.

25. Bruck, H.A.; McNeil, S.R.; Sutton, M.A.; Peter, W.H. Digital image correlation using Newton-Raphson method of partial differential correlation. *Experimental Mechanics* **1986**, 29(3), 261-268.

26. Kim, S.W.; Kim, N.S. Dynamic characteristics of suspension bridge hanger cables using digital image processing. *NDT & E International* **2013**, 59, 25-33.

27. Kim, S.W.; Lee, S.S.; Kim, N.S.; Kim, D.J. Numerical model validation for a prestressed concrete girder bridge by using image signals. *KSCE Journal of Civil Engineering* **2013**, 17(3), 509-517.

28. Rasmussen, B.P. Prediction interval estimation techniques for empirical modeling strategies and their applications to signal validation tasks. Ph.D. Dissertations, University of Tennessee, Knoxville, Tennessee, USA, December **2003**.

29. Robert, C. *Machine learning, a probabilistic perspective*. **2014**

30. Geman, S.; Bienestock, E.; Doursat, R.; Neural networks and the bias/variance dilemma. *Neural computation* **1992**, 4, 1-58.

31. James, G.M.; Variance and bias for general loss functions. *Machine Learning* **2003**, 51, 115-35.

32. Khosravi, A.; Nahavandi, S.; Creighton, D.; Atiya, A.F. Comprehensive review of neural network-based prediction intervals and new advances. *IEEE Transactions on neural networks* **2011**, 22, 1341-1356.

33. Barber, D. *Bayesian reasoning and machine learning*, Cambridge University Press. **2012**.

34. Rasmussen, C.E.; Williams, C.K. *Gaussian processes for machine learning*, MIT press: Cambridge, USA, **2006**.

35. Gubner, J.A. *Probability and random processes for electrical and computer engineers*, Cambridge University Press: Cambridge, USA, **2006**.

36. Petelin, D.; Grancharova, A.; Kociijan, J. Evolving Gaussian process models for prediction of ozone concentration in the air. *Simulation modelling practice and theory* **2013**, 33, 68-80.

37. di Sciascio, F.; Amicarelli, A.N. Biomass estimation in batch biotechnological processes by Bayesian Gaussian process regression. *Computers & Chemical Engineering* **2008**, 32, 3264-3273.

38. Likar, B.; Kocijan, J. Predictive control of a gas-liquid separation plant based on a Gaussian process model. *Computers & Chemical Engineering* **2007**, 31, 142-152.

39. Muirhead, R.J. *Aspects of multivariate statistical theory*, John Wiley & Sons: Hoboken, New Jersey, USA, **2009**.

40. Hyndman, R.J.; Koehler A.B. Another look at measures of forecast accuracy. *International Journal of Forecasting* **2006**, 22, 679-688.

41. Landberg, L. Short-term prediction of local wind conditions. *Journal of Wind Engineering and Industrial Aerodynamics* **2001**, 89, 235-245.

42. Sfetsos, A. A novel approach for the forecasting of mean hourly wind speed time series. *Renewable Energy* **2002**, 27, 163-174.

43. Odeha, I.O.A.; McBratney, A.B.; Chittleborough D.J. Spatial prediction of soil properties from landform attributes derived from a digital elevation model. *Geoderma* **1994**, 63, 197-214.

44. Shrivastava, N.A.; Khosravi, A.; Panigrahi, B.K. Prediction interval estimation of electricity prices using PSO-tuned support vector machines. *IEEE Transactions on Industrial Informatics* **2015**, 11, 322-331.

45. Lee, K.C.; Kim, S.I.; Hur, H.M.; Jeon, S.H. Evaluation of Traffic Safety and Passenger Comfort of KTX considering Vertical Deformation of Steel-Composite Arch Bridge due to Temperature Change. *Journal of the Korean Society for Railway* **2018**, 21(1), 47-54. (in Korean)

46. Nilson, A.H. *Design of Concrete Structures*, 13th Ed. New York, USA: McGraw-Hill **2003**.

47. Committee, A.C.I. Guide for modeling and calculating shrinkage and creep in hardened concrete. *ACI Committee 209* **2008**.

48. Korea Meteorological Administration. Available online: http://web.kma.go.kr/eng (accessed on 02 September **2017**).